

Effects of the torque model on the control of a VR spherical motor

Kok-Meng Lee^{a,*}, Raye A. Sosseh^b, Zhiyong Wei^a

^aGeorgia Institute of Technology, The George W. Woodruff School of Mechanical Engineering, MARC474, Atlanta, GA 303320405, USA

^bSeagate Technologies, Servo Engineering Technology, Oklahoma City, OK 73134, USA

Received 1 April 2003; accepted 17 July 2003

Abstract

This paper presents the effects of the torque model on the control of a variable reluctance spherical motor (VRSM) that offers several attractive features by combining multi-DOF motions in a single joint. A general form of the torque model for a VRSM is derived using the principle of energy conversion. The torque models for two specific design configurations developed at Georgia Tech are compared. The first has been based on an existing design characterized by a torque model in quadratic form. For feedback control of the spherical motor, the quadratic form of the torque model requires the use of nonlinear optimization schemes for computing the stator coil current inputs. The second design incorporating high coercive permanent magnets has a linear torque-current relationship and thus allows a closed form solution for both forward and inverse torque models. The effects of the torque model on a PD-controlled VRSM prototype has been studied both numerically and experimentally. Experimental results agree well with the computation derived analytically.

© 2003 Elsevier Ltd. All rights reserved.

Keywords: Actuator; Motor; Torque; Control; Electromagnetic; Finite element

1. Introduction

Multi-degree-of-freedom (DOF) actuators are finding increasing uses in a number of industries. The need for such systems has motivated the development of unconventional actuators that have a potential to realize multi-DOF motion in a single joint. One such actuator is a ball-joint-like spherical motor motivated by the rapid development of robotics in the 1980s.

In some applications such as high-speed plasma, laser or water-jet cutting, and coordinate-measuring, the demands on the workspace and wrist torque are low but the end-effector must be oriented quickly, continuously, and isotropically in all directions. A ball-joint-like motor characterized with no singularity in the middle of the workspace presents a major performance advantage in trajectory planning and control as compared to a popular three-consecutive-rotational-joint wrist. The ability of a spherical motor to provide continuous controlled spin motion while allow for some

regulation in roll and yaw motions offers several unique applications such as wheels for carving, steerable propeller, and rotating hands for live-object handling. Other potential applications include actuation for a three-DOF mechanical shoulder, an eyeball camera, as well as a robotic wrist. With the shoulder and the wrist joints driven by spherical motors and the elbow by a single-axis motor, only three actuators are needed for a total of seven DOFs. As compared to conventional robotic actuation, which would require 14 actuators in a dual arm manipulator system, a design using three-DOF actuators would significantly improve the kinematics and dynamic characteristics, and thus allow for more sophisticated intelligence to be implemented.

The three dominant types of spherical motors independently developed in the late 1980s are the induction type (Davey, Vachtsevanos, & Powers, 1987; Foggia, Oliver, & Chappuis, 1988), the variable reluctance (VR) motor that includes the stepper (Lee, Vachtsevanos, & Kwan, 1988), and the direct current motor (Hollis, Salcudean, & Allan, 1991; Kaneko, Yamada, & Ito, 1988). Lee and Pei (1991) investigated the kinematic relationship among the poles of a VRSM.

*Corresponding author. Tel.: +1-404-894-7402; fax: +1-404-894-9342.

E-mail address: kokmeng.lee@me.gatech.edu (K.-M. Lee).

The dynamic model of a particular VRSM can be found in (Lee, Roth, & Zhou, 1996), where the torque model is a quadratic function of the current inputs to the stator coils. More recently, Wang, Jewel, and Howe (1997) developed a similar VR spherical motor with a very simple magnetic rotor assembly and coil arrangement capable of two and three DOF motions. Chirikjian and Stein (1999) proposed a commutation algorithm for a spherical stepper. Of particular interest is the development of a VR spherical motor (VRSM), which possesses several advantages including smooth motion and compact in design. These, however, come with a number of challenges. To address some of the challenges, we offer the following:

1.1. A detailed analysis on the effects of the torque model on the VRSM control system is presented

A general form of the torque model for a VRSM is derived using the principle of energy conversion. The torque models for two specific design configurations (DC-I and DC-II) developed at Georgia Tech are compared. The first (or DC-I) has been based on an existing design (Lee et al., 1996) characterized by a torque model in quadratic form. For feedback control of the spherical motor, the quadratic form of the torque model requires the use of nonlinear optimization schemes for computing the stator coil current inputs. A look-up table is often used in order to reduce the computational load in real time. The desire to develop a VRSM that has a linear torque model has led to the development of DC-II incorporating high coercive permanent magnets. As will be demonstrated, since closed form solutions can be obtained from the inverse torque model, the sample time of the control system can be drastically reduced and kept as a constant.

1.2. The torque model of a VRSM has been computed using 3D finite element (FE) analysis

The motor designs to date have often been based on arguments employing rather simple magnetic circuits. Unlike prior studies where the torque models are often formulated using a lump-parameter approach, we derive the torque model from the magnetic field distributions using finite-element (FE) method. The torque generated by a VRSM depends on the magnetic field interaction between the stator electromagnets and the rotor poles. Using ANSYS, an off-the-shelf FE code, the torques were numerically predicted for the two design configurations. We verify the FE computation using DC-I. The 3D computation is then used to derive the torque model for DC-II.

1.3. The validity of the torque model on the VRSM control system has been tested both numerically and experimentally

Along with the torque model, a complete dynamic model that takes into account the effects of the orientation measurement system has been derived to serve as a design tool to simulate the dynamic performance of a PD-controlled VRSM system. Experiments conducted on a VRSM prototype shows that experimental results agree well with the computation derived analytically. The dynamic model that includes both forward and inverse torque models provides a useful platform for tuning of the controller gains of the VRSM control system.

1.4. We analyze the effects of the linear torque model on the control system performance of a VRSM through the number of control inputs

One of the most attractive features of a linear torque model is that a nonlinear input optimization is not necessary since a closed-form optimal solution can be derived. This unique feature offers a designer an additional flexibility to distribute the stator coils during the design stage. Unlike those with DC-I or DC-II where a small number of coils are used, the DC-III has 24 stator coils and 8 rotor permanent magnet poles. This stator–rotor layout is also characterized by having pairs of poles orthogonal to each other. Through a design simulation of a third design configuration (DC-III), we show that a linear torque model (which eases the use of large number of highly distributed inputs without the penalty of computational burdens) could result in much lower heat energy, which is dissipated during the transient.

2. Overview of the VRSM

The VRSM referred to in this paper has a similar structure as ball-joint-like device in (Lee et al., 1996). As shown in Fig. 1, the structure is made up of four basic assemblies, a spherical rotor, a hollow spherical stator, a bearing system, and an orientation measurement system. The stator houses a number of electromagnets strategically distributed on the inside of its surface. Similarly, the rotor consists of a number of poles made up of ferromagnetic materials or permanent magnets. The rotor poles radially meet at the center of the rotor, and the stator cores are connected by the magnetic conductor layer in the stator shell to form a magnetic circuit with the air gaps.

Feedback control of the spherical motor requires an orientation measurement system. When off-the-shelf single-axis encoders are used, a typical orientation measurement system requires a mechanism that consists

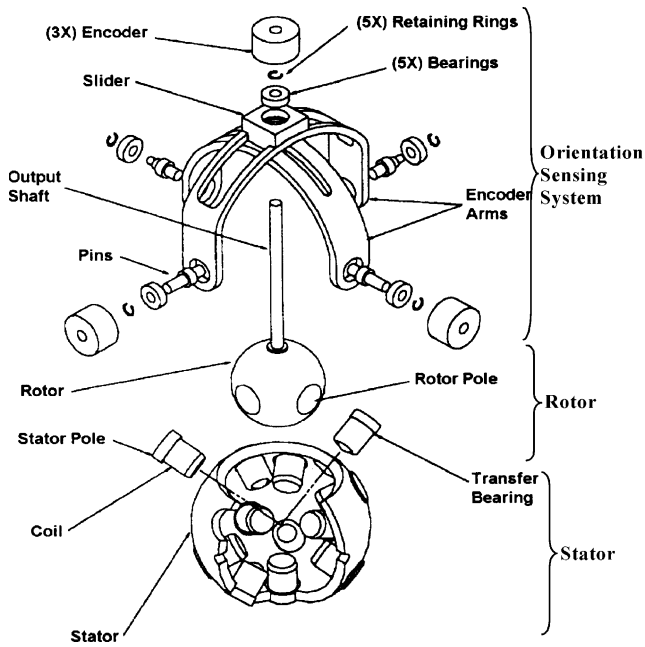


Fig. 1. Explored view of a VRSM CAD model.

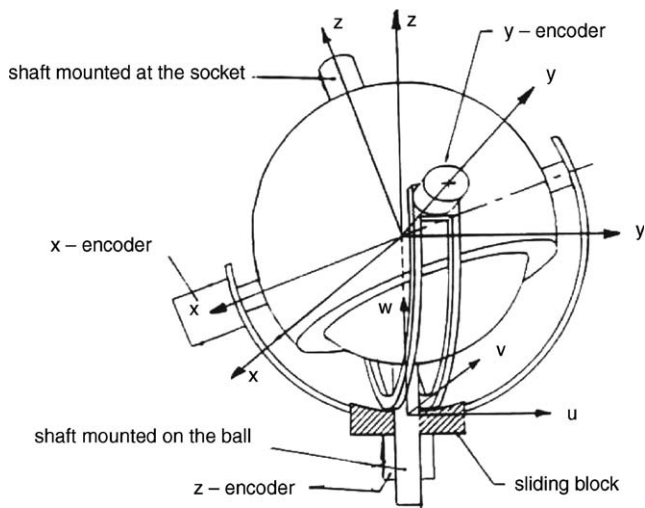


Fig. 2. Orientation mechanism.

of the two arc-shaped guides and a sliding block. The two guides are mounted orthogonally on bearing pins attached to the outside of the stator. As shown in Fig. 2, the X and Y encoders measure the rotation of their corresponding guides and the Z encoder measures the spin of the rotor shaft about its axis. Detailed derivations of the kinematics that relate the encoder readings $(\theta_x, \theta_y, \theta_z)$ to the rotor orientation or the ZYZ Euler angles (ψ, θ, ϕ) can be found in (Lee & Pei, 1991). The forward kinematics is given below:

$$\psi = \text{atan } 2(-S_{t_y}, C_{t_y} S_{\theta_y}), \tag{1a}$$

$$\theta = \text{atan } 2(S_{\theta_y}, C_{\theta_y} C_{\psi}), \tag{1b}$$

$$\phi = \text{atan } 2(S_{\theta_y} S_{\theta_{zy}} + C_{\theta_z} S_{t_y} C_{\theta_y}, S_{\theta_y} C_{\theta_z} - S_{\theta_z} S_{t_y} C_{\theta_y}), \tag{1c}$$

where $C_{(\bullet)} = \cos(\bullet)$; $S_{(\bullet)} = \sin(\bullet)$; and $t_y = \text{atan } 2(-S_{\theta} S_{\psi} C_{\theta_y}, C_{\theta})$. $\tag{2}$

The corresponding inverse kinematics is

$$\theta_x = \text{atan } 2(-S_{\theta} S_{\psi}, C_{\theta}), \tag{3a}$$

$$\theta_y = \text{atan } 2(S_{\theta} C_{\psi}, C_{\theta}), \tag{3b}$$

$$\theta_z = \text{atan } 2(C_{\phi} C_{\theta} S_{\psi} + S_{\phi} C_{\psi}, -S_{\phi} C_{\theta} S_{\psi} + C_{\phi} C_{\psi}). \tag{3c}$$

The control of a VRSM consists of two steps as shown in Fig. 3. First, a stabilizing torque is designed to control the VRSM along a desired trajectory. Next, since the motor has redundant inputs, the currents required to generate the stabilizing torque designed in the first step are determined by solving a constrained optimization problem. As will be shown in the following sections, the torque and dynamic models have significant effects on the control of the VRSM.

3. Torque model

The spherical motor magnetic co-energy can be expressed in the following quadratic form:

$$W_c = \frac{1}{2} \mathbf{I}^T [\mathbf{L}] \mathbf{I}, \tag{4}$$

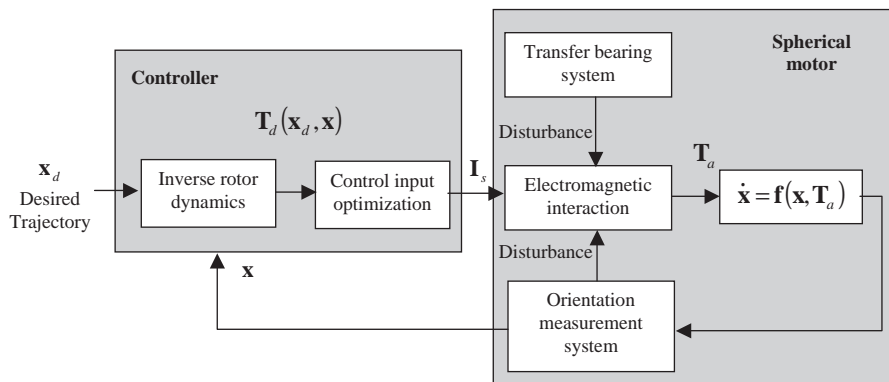


Fig. 3. Structure of the VRSM controlled system.

where

$$[L] = \begin{bmatrix} [L_{ss}] & [L_{sr}] \\ [L_{rs}] & [L_{rr}] \end{bmatrix}, \quad \mathbf{I} = \begin{bmatrix} \mathbf{I}_s \\ \mathbf{I}_r \end{bmatrix},$$

where \mathbf{I}_s and \mathbf{I}_r are the stator and rotor current input vectors, respectively; $[L_{ss}]$ and $[L_{rr}]$ are the self-inductance sub-matrices of the stator and rotor, respectively; and $[L_{sr}] = [L_{rs}]^T$ is the mutual inductance sub-matrix. The matrix, $[L] \in \mathfrak{R}^{(m+n) \times (m+n)}$, where m and n are the number of electromagnets and rotor poles respectively, is therefore symmetric. The torque can be derived by differentiating the magnetic co-energy with respect to the angular position variables $T_l = (\partial W'_m / \partial \theta_l)$, where $l = 1, 2$ and 3 corresponding the axes x , y , and z , respectively. Note that permanent magnets (PMs) can be modeled as an equivalent magneto-motive force (mmf) or Ampere-turns. In general, the VR spherical motor torque has the following form:

$$T_l = \frac{1}{2} \mathbf{I}_s^T \frac{\partial [L_{ss}]}{\partial \theta_l} \mathbf{I}_s + \frac{1}{2} \mathbf{I}_r^T \frac{\partial [L_{rr}]}{\partial \theta_l} \mathbf{I}_r + \mathbf{I}_r^T \frac{\partial [L_{rs}]}{\partial \theta_l} \mathbf{I}_s. \quad (5)$$

3.1. Effects of pole design on motor torque

The specific form of the torque depends on the design of the stator and rotor poles. Two specific design configurations, both of which share similar mechanical structure with a rotor diameter of 76.2 mm, are compared below.

3.1.1. Design configuration I (DC-I)

In this configuration, stator electromagnetic coils are wound on ferromagnetic cores. Rotor poles are simple iron cores with no excitation (or $\mathbf{I}_r = 0$). The spherical motor torque has a strictly quadratic form (Lee et al., 1996):

$$T_l = \frac{\partial W'_m}{\partial \theta_l} = \frac{1}{2} \mathbf{I}_s^T \frac{\partial [L_{ss}]}{\partial \theta_l} \mathbf{I}_s. \quad (6)$$

The specific prototype developed at Georgia Tech has eleven electromagnets of 500 turns arranged following the pattern of a regular icosahedron while the rotor houses five iron poles located at the vertices of a regular octahedron. The topmost stator and rotor poles are

eliminated to provide area for the shaft as shown in Fig. 1.

3.1.2. Design configuration II (DC-II)

An alternative configuration is to replace the rotor poles with permanent magnets. A particular design with six cylindrical PMs is shown in Fig. 4(a), where the magnetization axes of the PMs are arranged such that adjacent PMs have opposite polarity. The PMs are then molded as a part of a smooth spherical ball as shown in Fig. 4(b). In addition, in order to have no generated torque when there are no current excitations, the stator coils of 1000-turns are wound on non-ferromagnetic cores, the result of which is eliminating the third term in Eq. (5). The removal of the ferromagnetic core reduces the self-inductance $[L_{ss}]$ of the electromagnetic coils and hence the contribution to the first term of Eq. (5). When the self-inductance term is small compared to the second term due to mutual-inductance term, the torque can be approximated by a linear combination of stator input currents:

$$T_l \approx \mathbf{I}_r^T \frac{\partial [L_{rs}]}{\partial \theta_l} \mathbf{I}_s = [K(\mathbf{q})] \mathbf{I}_s, \quad (7)$$

where \mathbf{I}_r is a vector characterizing the equivalent currents of the given PMs; and $\mathbf{q} = [\psi, \theta, \phi]^T$ is a vector of ZYZ Euler angles describing the rotor orientation w.r.t. the stator reference frame.

3.2. Finite-element modeling of motor torque

The torque model of a spherical motor is a function of magnetic field distribution governed by Maxwell's equations:

$$\nabla \cdot \mathbf{B} = 0, \quad (8a)$$

$$\nabla \times \mathbf{H} = \mathbf{J}, \quad (8b)$$

where \mathbf{H} is the magnetic field intensity; \mathbf{J} is the current density; and $\mathbf{B} = \mu \mathbf{H}$ is the magnetic flux density. Closed form solutions to these equations are rather cumbersome and are only available for a few devices with relatively simple structures.

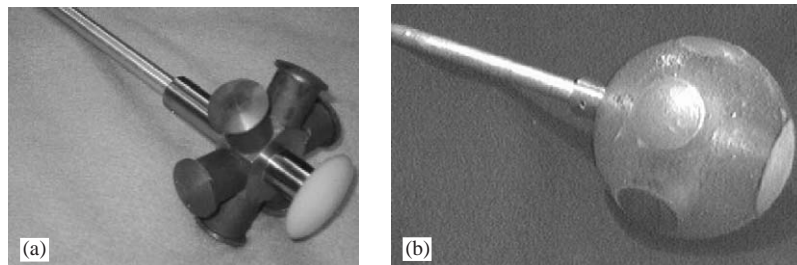


Fig. 4. Rotor of DC-II. (a) Before molding. (b) After molding.

3.2.1. Finite element formulation using scalar potential

Maxwell's equations that govern the spherical motor field distribution are formulated using scalar potential functions and solved using FE methods. Using scalar potential formulation, the magnetic field intensity is separated into two parts, $\mathbf{H} = \mathbf{H}_s + \mathbf{H}_m$, where \mathbf{H}_s and \mathbf{H}_m are the field intensity due to the current source and the magnetization of the material, respectively. \mathbf{H}_s is solved using the Biot-Savart law:

$$\mathbf{H}_s = \frac{1}{4\pi} \int_V \frac{\mathbf{J} \times \mathbf{r}}{|\mathbf{r}|^3} dV, \quad (9)$$

where \mathbf{r} is the position vector from current source to a node point, and V is the volume of the current source. \mathbf{H}_m is curl free and expressed in terms of a scalar potential function Φ :

$$\mathbf{H}_m = -\nabla\Phi. \quad (10)$$

Using constitutive relationship and Eq. (10), Eq. (8a) can be written as

$$\nabla \cdot (\mu \nabla \Phi) = 0 \quad (11)$$

which is commonly referred to as Laplace's equation. Once the magnetic field distribution is known, the torque generated by the spherical motor can be computed using Eq. (12):

$$\mathbf{T} = - \int_V \mathbf{a} \times (\mathbf{J} \times \mathbf{B}) dV, \quad (12)$$

where $(\mathbf{J} \times \mathbf{B})$ is the Lorentz force; \mathbf{a} represents the moment arm perpendicular to the axis of rotation and directed to the point where the force is computed.

In formulating the magnetic field distribution of the spherical motor, the space occupied by the motor is divided into four regions as shown in Fig. 5 where A and C are the typical flux surface and contour respectively. ANSYS, an off-the-shelf FE analysis package, is used to solve for the potential function. The SOLID96 element (an eight-node brick element with six DOF) in ANSYS is used to model the interior regions of the spherical motor. The six DOF include displacement, electric

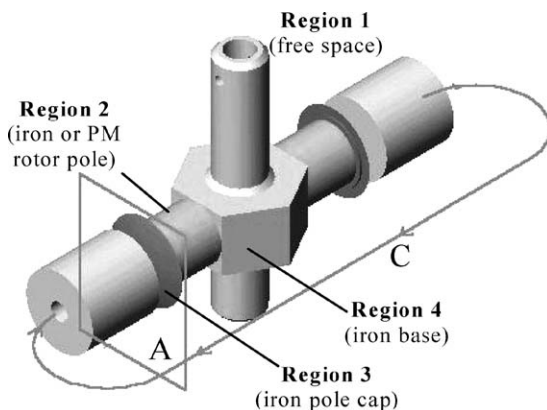


Fig. 5. FE model.

potential, magnetic scalar potential, and temperature. The exteriors of the free space (air) regions are modeled using INFIN47 elements. These four-node boundary elements model the far field decay in the magnetic field. The coil regions of the spherical motor are represented by SOURCE36 elements. Since the ANSYS FE package does not provide torque as an output, a macro was written to compute the torque generated by summing the cross products of the elemental force with its centroid.

3.2.2. FE torque analysis and model

The FE analysis consists of two parts. The first part is to verify the computation using published experimental data performed on the DC-I. Next, the FE torque model is derived for the DC-II (Sosseh, 2001).

3.2.2.1. Verification using DC-I. Some experimental measurements were conducted with DC-I (Lee et al., 1996) to model the permeance between an adjacent pair of stator and rotor poles. In (Lee et al., 1996), DC-I was assembled with two electromagnets spaced 180 degrees apart such that the axes of the two stator poles align with two of four cylindrical rotor poles. The torque generated by the magnetic interaction was measured using a six-DOF force/torque sensor. A series of torque measurements was then taken with the rotor's position and the stator pole current inputs as independent variables. An FE analysis of the above experiment is performed for current inputs of 1 and 2 A with separation angles ranging from 0° to 90° in six-degree increments. Due to the iron losses in the experiments, all iron regions in the FE analysis are represented by the BH curve in Fig. 6(a). Both Roth's experiments and the FE analysis show that the torque generated by DC-I has the following form:

$$T(\varphi) = K(\varphi)i^2, \quad (13)$$

where T is the resultant of the measured torque; φ is the separation angle between a pair of interacting poles; K is an equivalent "torque constant" function of φ ; and i is the current applied to the stator electromagnets. Fig. 6(b) compares the FE computation of $K(\varphi)$ for 1 and 2 A. As shown in Figs. 6(c) and (d), the FE results agree with the data obtained experimentally.

3.2.2.2. Torque model of DC-II. The torque model for DC-II has been derived using FE methods (see Fig. 7). If superposition holds, the complete spherical motor torque model can be derived from the one-pole pair torque model. The principles of superposition should be held if the first and third terms in the torque model given by Eq. (5) are negligible. This results from removing the iron core in the stator coils. By evaluating the torque that results from the interaction of one stator pole pair with two rotor pole-pairs, and comparing these results

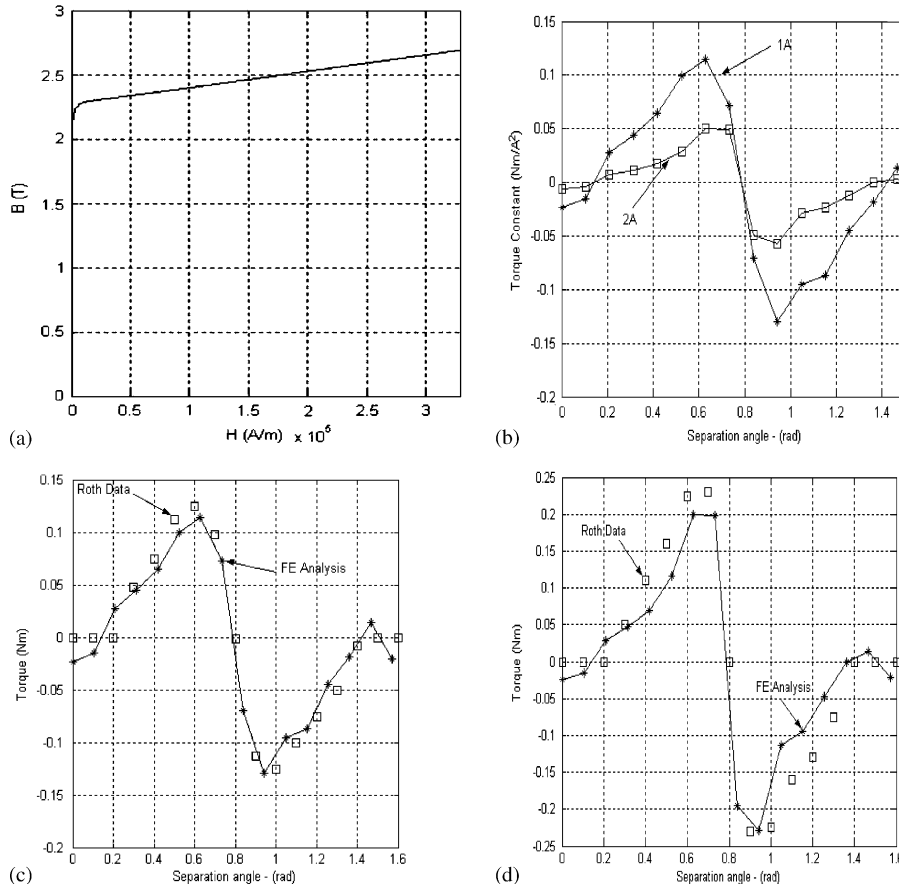


Fig. 6. Verification of FE computation using DC-I. (a) BH curve of 1010 steel core, (b) FE computed data, (c) Comparison $I=1\text{ A}$, (d) Comparison $I=2\text{ A}$.

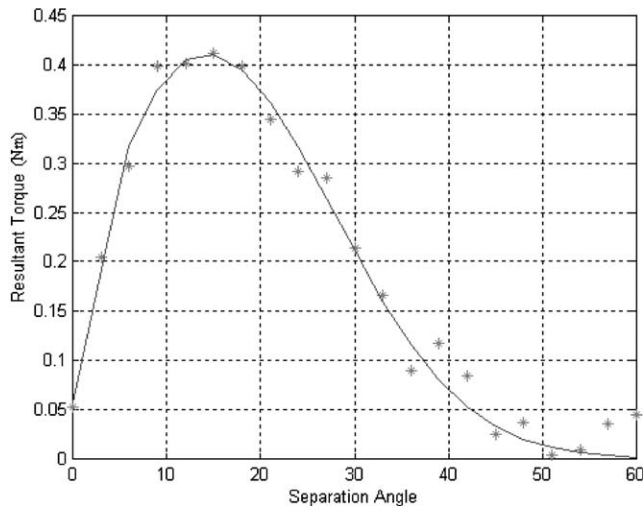


Fig. 7. FE computed torque data.

with the torque obtained by summing up results from individual pole pair interactions, the principles of superposition can be verified.

As suggested by the Lorentz force computed numerically, the torque generated by the interaction between a pair of rotor–stator poles can be written in the

following form:

$$T_{jk} = -f(\varphi_{jk}) \frac{s_j \times r_k}{|s_j \times r_k|} i_j, \tag{14}$$

where $f(\varphi_{jk})$ is a torque constant; s_j is the location vector of the stator coil; and r_k is the magnetization axis of the rotor pole.

Using a radial basis transfer function, the approximate torque constant $\hat{f}(\varphi_{jk})$ derived from the FE computed data shown in Fig. 7 has the following form:

$$\hat{f}(\varphi_{jk}) = \frac{\|T_{jk}\|}{i_j} = \sum_{n=1}^{N_f} \alpha_n \exp(-\lambda_n \varphi_{jk}^2), \tag{15}$$

where the estimation coefficients α_n and λ_n are determined such that the norm squared of the estimation error— $\|f(\varphi_{jk}) - \hat{f}(\varphi_{jk})\|^2$ is minimized; and N_f is the order of the estimation function. Fig. 7 shows the torque constant from the ANSYS simulations against the approximate torque constant. The coefficients for the approximate function with $N_f = 4$ are $\lambda_1 = 8.02$; $\lambda_2 = 7.85$; $\lambda_3 = 38.90$; $\lambda_4 = 176.61$; $\alpha_1 = -35.62$; $\alpha_2 = 35.89$; $\alpha_3 = 0.10$; and $\alpha_4 = -0.28$. In the approximate model, the torque from the interaction of a pair of poles is set to zero for separation angles larger than 40° , since the

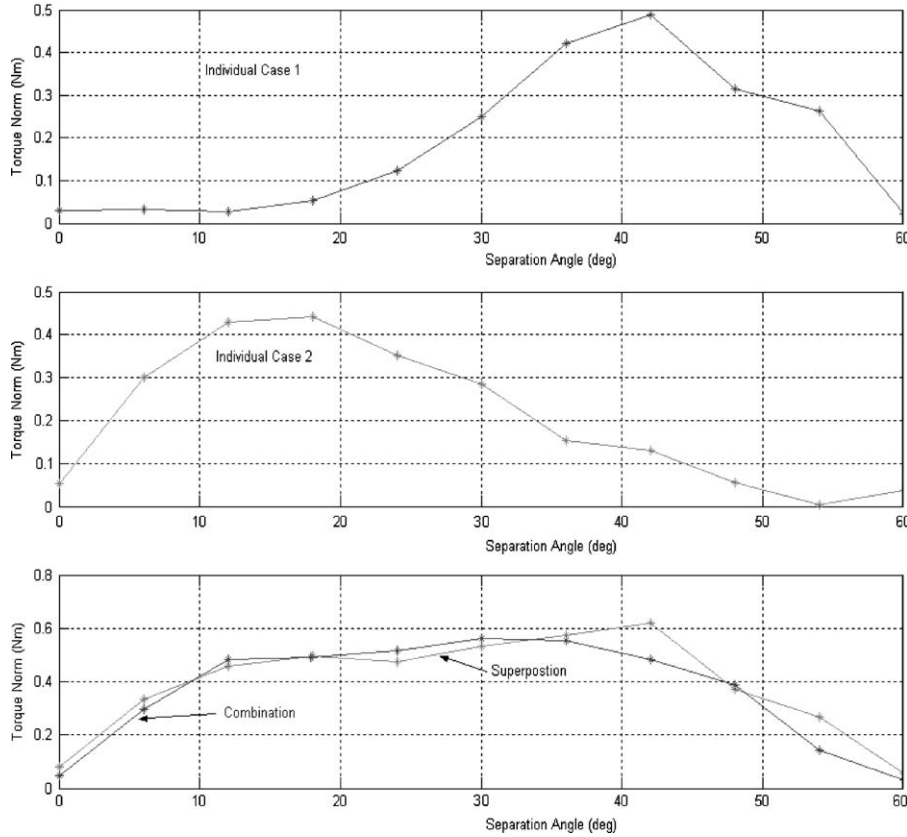


Fig. 8. Superposition of motor torques.

generated torque beyond this separation angle is smaller than the error due to the mesh size.

Since the torque model developed so far is valid only for the interaction of one pair of poles, an additional test was performed to determine if the principles of superposition hold. Fig. 8 shows simulation results for verifying that superposition holds. The superposition of the two individual cases came very close to the case with the combined rotor poles. This implies that the torque generated by the interaction of one stator pole pair with N rotor pole pairs is similar to summing up the interaction of N one-pole pair interactions. Therefore the torque generated by the interaction of one stator pole pair and N rotor pole pairs can be evaluated as follows:

$$\widehat{T}_{jN} = \sum_{k=1}^N \widehat{f}(\varphi_{jk}) \frac{s_j \times r_k}{\|s_j \times r_k\|} i_j. \quad (16)$$

4. Dynamic model of the motor/sensor system

The orientation measuring system contributes two-thirds of the total system inertia and cannot be neglected. The effects of the X - and Y -guides on the

rotor dynamics can be described by the constraint equations in the following form:

$$f_1(q^T; \theta_X, \theta_Y) = 0, \quad (17a)$$

$$f_2(q^T; \theta_X, \theta_Y) = 0, \quad (17b)$$

where $q^T = [\psi, \theta, \phi]$. To include the constraints imposed by the X - and Y -guides, we use a Lagrange formulation to derive the dynamic model for the combined rotor and encoder mechanism:

$$\frac{d}{dt} \left(\frac{\partial L}{\partial \dot{q}_j} \right) - \frac{\partial L}{\partial q} = Q_j + \sum_{i=1}^2 a_{ij} \lambda_i, \quad (18)$$

where $J = 1, \dots, 5$; L is Lagrangian; Q_j represents the applied torque; λ_1 and λ_2 are constrained Lagrange multipliers; and the term $\sum_{i=1}^2 a_{ij} \lambda_j$ represents the contribution of the reaction forces (from the measurement guides) to the generalized moments. In Eq. (18), a_{ij} are the elements of the Jacobian matrix $[a] = \begin{bmatrix} [a_r] & [I] \end{bmatrix}$ of the angular velocity constraints, which can be derived by differentiating Eqs. (17a) and (17b), in the following form:

$$\begin{bmatrix} [a_r] & [I] \end{bmatrix} \begin{bmatrix} q \\ \theta_X \\ \theta_Y \end{bmatrix} = \begin{bmatrix} 0 \\ 0 \end{bmatrix}, \quad (19)$$

where $[a_r]$ is a 3×2 matrix, the elements of which are functions of the ZYZ Euler angles; and $[I]$ is a 2×2 identity matrix. It can be shown that the dynamic model of the combined rotor/sensor mechanism can be written in the following compact form:

$$\dot{\mathbf{x}}_1 = \mathbf{x}_2, \quad (20)$$

$$[H(\mathbf{x}_1)]\dot{\mathbf{x}}_2 = \mathbf{T}(\mathbf{x}_1, \mathbf{u}) - \mathbf{C}(\mathbf{x}_1, \mathbf{x}_2), \quad (21)$$

where $\mathbf{x}_1 = q$ and $\mathbf{x}_2 = \dot{q}$ are 3×1 vectors of the ZYZ Euler angles (ψ, θ, ϕ) and their velocities respectively; $[H(\mathbf{x}_1)]$ is a symmetric, positive-definite inertia matrix given by

$$[H(\mathbf{x}_1)] = [B(\mathbf{x}_1)]^{-1}[[J_r] + [a_r^T][J_g][a_r]] \quad (22)$$

and $\mathbf{C}(\mathbf{x}_1, \mathbf{x}_2)$ represents the vector of Coriolis terms given by

$$[\mathbf{C}(\mathbf{x}_1, \mathbf{x}_2)] = [B(\mathbf{x}_1)]^{-1}[\tau + [a_r^T][J_g][a_r]]$$

and where

$$[B(\mathbf{x}_1)] = \begin{bmatrix} -S_\theta C_\theta & S_\theta S_\phi & C_\theta \\ S_\phi & C_\phi & 0 \\ 0 & 0 & 1 \end{bmatrix}, \quad (24)$$

$$[J_r] = \begin{bmatrix} (I_2 - I_1)\cos^2 \theta + I_1 & 0 & I_2 \cos \theta \\ 0 & I_1 & 0 \\ I_2 \cos \theta & 0 & I_2 \end{bmatrix}, \quad (25)$$

$$[J_g] = \begin{bmatrix} I_{Xg} & 0 \\ 0 & I_{Yg} \end{bmatrix}, \quad (26)$$

$$[a_r] = \begin{bmatrix} \frac{-S_\theta C_\theta C_\psi}{S_\theta^2 S_\psi^2 + C_\theta^2} & \frac{-S_\psi}{S_\theta^2 S_\psi^2 + C_\theta^2} & 0 \\ \frac{S_\theta C_\theta C_\psi}{S_\theta^2 C_\psi^2 + C_\theta^2} & \frac{-C_\psi}{S_\theta^2 C_\psi^2 + C_\theta^2} & 0 \end{bmatrix}, \quad (27)$$

$$\tau = \begin{bmatrix} 2(I_2 - I_1)S_\theta C_\theta \dot{\psi} \dot{\theta} + I_2 S_\theta \dot{\theta} \dot{\phi} \\ (I_1 - I_2)S_\theta C_\theta \dot{\psi}^2 - I_2 S_\theta \dot{\psi} \dot{\phi} \\ I_2 S_\theta \dot{\psi} \dot{\theta} \end{bmatrix}. \quad (28)$$

5. Control system experiments

The VRSM prototype DC-II developed at Georgia Tech has been used to test the effects of the torque model of the VRSM controlled system. The test bed is shown in Fig. 9.

5.1. Control algorithms

As shown in Fig. 3, the control algorithm is designed in two stages. In the first stage, the desired stabilizing torque \mathbf{T}_d is first determined as the fictitious control input. In the second stage, the optimal control input vector \mathbf{u} is determined. The problem of finding the actual control input vector \mathbf{u} from the fictitious control input vector \mathbf{T}_d is set up as a static constraint optimization problem. The actual current input vector is found by minimizing the control input energy consumption:

$$J = \frac{1}{2} \mathbf{u}^T [W] \mathbf{u} \quad (29)$$

subject to the desired torque constraint

$$\mathbf{T}_d(\mathbf{x}_1) = [K_t(\mathbf{x}_1)] \mathbf{u}, \quad (30)$$

where $\mathbf{u} \in R^{10}$ is the control vector of stator coil currents; and $[W] \in R^{10 \times 10}$ is a positive definite weighting matrix. Provided that the control currents are kept within limits, the optimal solution to this problem can be solved using Lagrange multipliers. The optimal solution can be written in closed form:

$$\mathbf{u} = [W]^{-1} [K_t^T] [[K_t][W]^{-1} [K_t^T]]^{-1} \mathbf{T}_d. \quad (31)$$

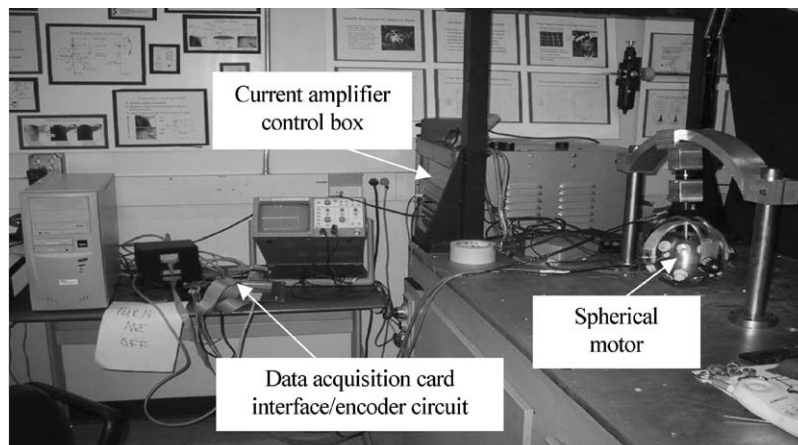


Fig. 9. VRSM control system test bed.

In implementation, saturation limits are imposed on the controller to ensure the current inputs are within the amplifier limitations. The eventual stability of the system depends on whether the spherical motor can generate the desired torque.

Two different formulations of stabilizing torques are considered for the first stage of the controller; namely, a PD controller and a back-stepping controller.

5.1.1. PD controller

Using Lyapunov stability analysis, it can be readily shown that the desired torque for a PD controller,

$$\mathbf{T}_d = [K_p]\tilde{\mathbf{x}}_1(\mathbf{t}) + [K_d]\tilde{\mathbf{x}}_2(\mathbf{t}), \tag{32}$$

where $\tilde{\mathbf{x}}_1(\mathbf{t}) = \mathbf{q}_d - \mathbf{q}(\mathbf{t})$ and $\tilde{\mathbf{x}}_2(\mathbf{t}) = \dot{\mathbf{q}}_d - \dot{\mathbf{q}}(\mathbf{t})$ define the orientation tracking error and its derivative, respectively, can drive the VRSM from its initial state to a specified final state.

5.1.2. Back-stepping controller

The cascaded spherical motor dynamics in Eqs. (20) and (21) have the appropriate structure for the back-stepping controller design method. The desired torque for a back-stepping controller has the following form:

$$\mathbf{T}_d = [H(\mathbf{x}_1)]\mathbf{y} + \mathbf{C}(\mathbf{x}_1, \mathbf{x}_2). \tag{33}$$

Eq. (33) is a nonlinear compensator since it depends on the dynamics of the spherical motor, where \mathbf{y} is derived such that the rotor will track the desired specified state \mathbf{x}_{1d} if the position error dynamics are given as follows:

$$\dot{\tilde{\mathbf{x}}}_1 + [K_p]\tilde{\mathbf{x}}_1 = 0, \tag{34}$$

where $\tilde{\mathbf{x}}_1 = \mathbf{x}_{1d} - \mathbf{x}_1$ and $[K_p]$ is a positive-definite gain matrix. Eq. (34) can be rewritten as

$$\mathbf{x}_2 = \dot{\mathbf{x}}_{1d} + [K_p]\tilde{\mathbf{x}}_1. \tag{34a}$$

Substituting the fictitious control input \mathbf{x}_{2d} for \mathbf{x}_2 in Eq. (34a) yields

$$\mathbf{x}_{2d} = \dot{\mathbf{x}}_{1d} + [K_p](\mathbf{x}_{1d} - \mathbf{x}_1). \tag{35}$$

The fictitious control input \mathbf{x}_{2d} is selected as the specified velocity trajectory leading to the velocity error $\tilde{\mathbf{x}}_2 = \mathbf{x}_{2d} - \mathbf{x}_2$. The error dynamics in Eq. (36) ensures the velocity error approaches zero asymptotically, which will eventually lead to the asymptotic convergence of the rotor position error.

$$\dot{\tilde{\mathbf{x}}}_2 + [K_d]\tilde{\mathbf{x}}_2 = 0, \tag{36}$$

where $[K_d]$ is a positive-definite gain matrix. Eq. (36) can be rewritten as

$$\dot{\mathbf{x}}_2 = \dot{\mathbf{x}}_{2d} + [K_d]\tilde{\mathbf{x}}_2. \tag{36a}$$

Substituting Eq. (36a) into Eq. (21) leads to the stabilizing torque:

$$\mathbf{T}_d = [H](\dot{\mathbf{x}}_{2d} + [K_d]\tilde{\mathbf{x}}_2) + \mathbf{C}(\mathbf{x}_1, \mathbf{x}_2). \tag{37}$$

Comparing Eqs. (37) and (33) leads to

$$\begin{aligned} \mathbf{y} &= \dot{\mathbf{x}}_{1d} + [K_p](\dot{\mathbf{x}}_{1d} - \dot{\mathbf{x}}_1) + [K_d] \\ &\quad \times \{[\mathbf{x}_{1d} + [K_p](\mathbf{x}_{1d} - \mathbf{x}_1)] - \dot{\mathbf{x}}_1\} \end{aligned}$$

or
$$\mathbf{y} = \dot{\mathbf{x}}_{1d} + ([K_p] + [K_d])(\dot{\mathbf{x}}_{1d} - \dot{\mathbf{x}}_1) + [K_p][K_d](\mathbf{x}_{1d} - \mathbf{x}_1). \tag{38}$$

5.2. Simulation and experimental results

The PD gains of the VRSM were tuned via numerical simulation and examined experimentally. Fig. 10 shows the simulation results comparing three different gains, where the VRSM is commanded to move from $(\theta_X = \theta_Y = \theta_Z = 0^0)_i$ to $(\theta_X = 0^0, \theta_Y = 10^0, \theta_Z = 60^0)_d$. The simulations correspond to a proportional controller gain of $[K_p] = \text{diag}(500, 200, 500)$ and a derivative gain of $[K_d] = \text{diag}(50, \alpha, 12.5)$, with $\alpha = 15, 25, \text{ and } 50$. With $[K_p] = 500[I]$ and $[K_d] = 15[I]$, a significant steady state error results in θ_Y .

Experimental results are given in Fig. 11, which were obtained with the controller gains, $[K_p] = \text{diag}(500, 200, 500)$ and $[K_d] = \text{diag}(50, 50, 12.5)$. Fig. 11 shows the input currents and the corresponding torque components for $\alpha = 50$. In Fig. 11(b), the applied currents result from the application of a current amplitude saturation limit of 3.25 A on the desired currents to match the current limit imposed by the amplifiers. Figs. 11(a) and (b) show that the desired currents for the PD controller are much lower than the saturation limit at almost all times; the desired and applied currents are equivalent. These simulation results show that the spherical motor can successfully reach the specified point from its initial upright position.

It is worth noting that due to the symmetric arrangement of the spherical motor coils, the currents

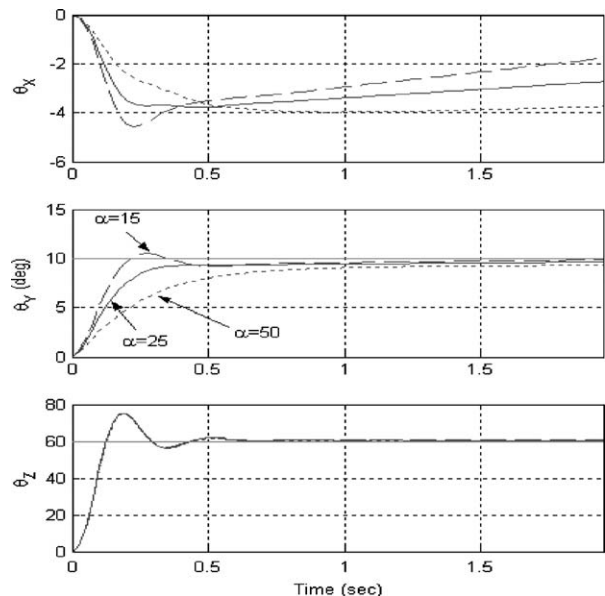


Fig. 10. Simulation results ($\alpha = 15, 25$ and 50).

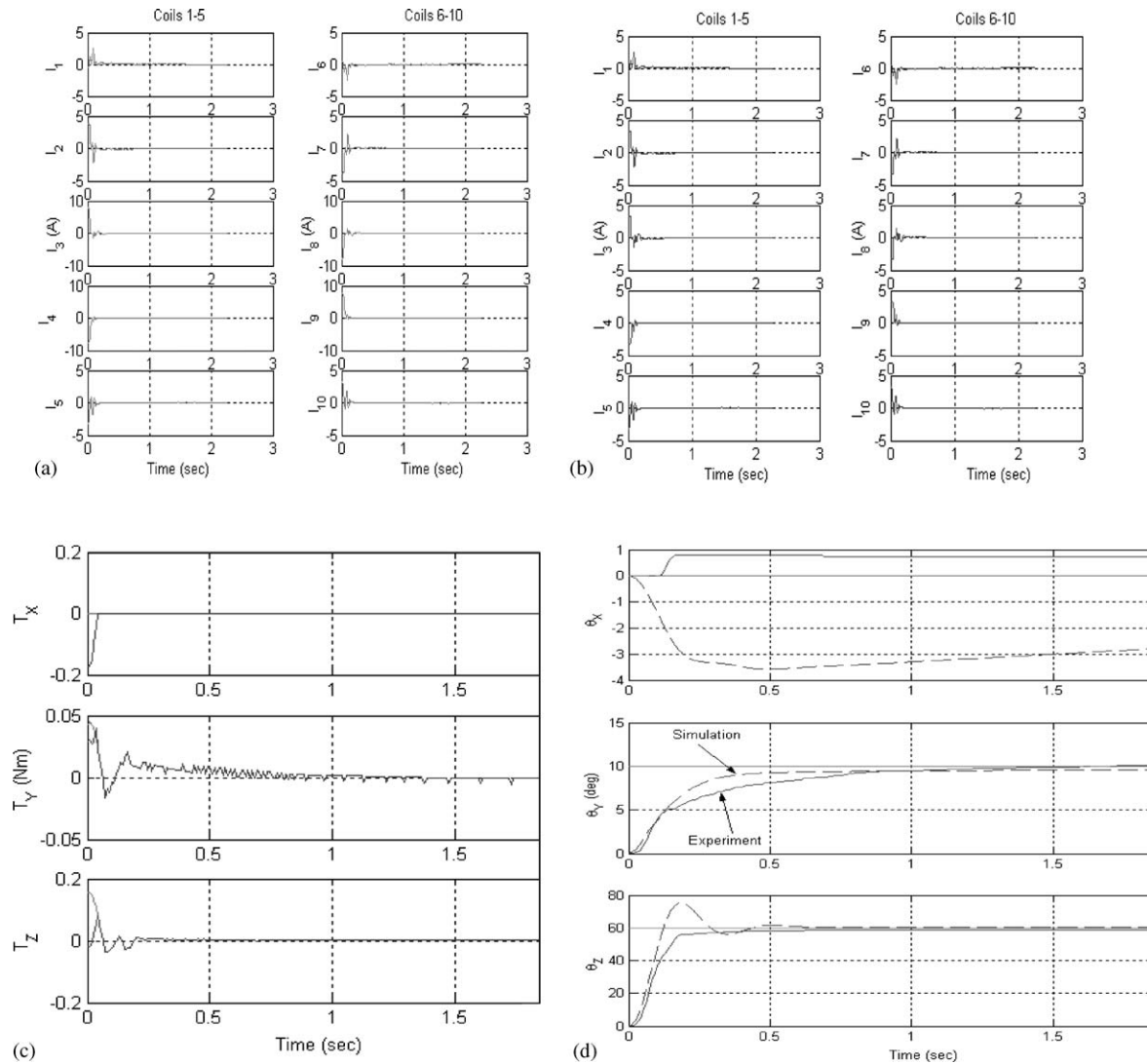


Fig. 11. Experimental results ($\alpha = 50$). (a) Desired currents. (b) Applied currents. (c) Desired and applied torque. (d) Comparison of results (simulation vs. experimental).

in stator coils #6 through #10 are equal but opposite in direction to the currents in coils #1 through #5. In addition, since the applied current and desired current are identical, the applied torque \mathbf{T} computed (using the optimized current) agrees very well with the desired torque \mathbf{T}_d (fictitious control input) as shown in Fig. 11(c). The experimental results are compared against the simulation in Fig. 11(d), which shows good agreement. These results validate both the torque model and the VRSM dynamics presented in Sections 3 and 4, respectively. The simulation algorithm developed here can therefore be used as an effective design tool for proper selection of the feedback controller gains.

6. Design simulation

The torque model of DC-II is a linear function of stator coil currents; a nonlinear input optimization is

not necessary since Eq. (31) offers a closed form solution. This unique feature allows the use of a large number of stator coils with no added complexity in computing an optimal set of input currents. It is thus of interest to explore how the linearity of the torque model could influence the control system performance of a VRSM through the number of control inputs. The transient response of the motor can be further improved by using non-contact optical measuring sensor instead of the current encoder guides and reducing the rotor inertia. This kind of 3D measuring system is now under development in Georgia Tech. For this reason, we simulate the motion of an alternative design configuration DC-III (which has 24 stator coils and 8 rotor PM poles) with and without encoder guide mechanism against that of the DC-II using a back-stepping controller given by Eqs. (33) and (38).

Table 1
Values used in design simulation

	Dc-II	Dc-III
Stator coils	10, ID = 9.53 mm, OD = 25.4 mm	24, ID = 5.72 mm, OD = 15.24 mm
Coil wire diameter	0.406 mm	0.3175 mm
Coil resistance	6.8 Ω	6.46 Ω
Magnetization axes	$\pm 26^\circ$	$\pm 15^\circ$
Rotor PM poles	6, diameter = 19.1 mm	8, diameter = 11.4 mm

Unlike those with DC-I or DC-II where only two coils are diametrically placed on each of five evenly spaced great circles, the coils in DC-III are radially located symmetrically above and below the XY plane and evenly distributed circumferentially such that there are four stator coils in each of the 6 evenly distributed great circles. With this arrangement, the two pairs of diametrically placed stator coils of the DC-III can generate both positive and negative torques in a plane. The 24-8 stator-rotor layout is also characterized by having pairs of poles orthogonal to each other. While lower currents can be used with a larger number of coils and a more distributed nature of the pole arrangement for a specified torque, the trade-off is that the motion range is limited for the same rotor size of 76.2 mm diameter. In addition, a smaller diameter of coil wire is used in order to maintain the same number of turns of 1000.

The step responses of the two designs were simulated for the command to move the rotor from $(\theta_X = \theta_Y = \theta_Z = 0^\circ)_i$ to $(\theta_X = 15^\circ, \theta_Y = 0^\circ, \theta_Z = 60^\circ)_d$ with a back-stepping controller for the following cases:

- Case 1: DC-II with controller gains of $[K_p] = \text{diag}(10, 30, 40)$ and $[K_d] = \text{diag}(25, 25, 12.5)$.
- Case 2: DC-III with the same controller gains as Case 1.
- Case 3: DC-III with no encoder guide mechanism and controller gains of $[K_p] = \text{diag}(20, 120, 80)$ and $[K_d] = \text{diag}(37.5, 25, 18.5)$.

Table 1 summarizes and compares the values of the design parameters used in the simulation. The geometrical similarity of the stator coils and the rotor PM poles between the two designs is maintained so that the FE torque data curve in Fig. 7 obtained for the DC-II can be scaled for the DC-III.

Fig. 12 compares the step responses for the three cases, where the corresponding torque is given in Fig. 13. Fig. 14 compares the total heat power generated by the currents flowing through all the coils during the transient. As compared in Fig. 12, the performance of DC-III is superior to that of DC-II in terms of overshoot and response time, particularly the case with no encoder guide mechanism. The results can be best explained using Fig. 13. Fig. 13(a) shows that there are

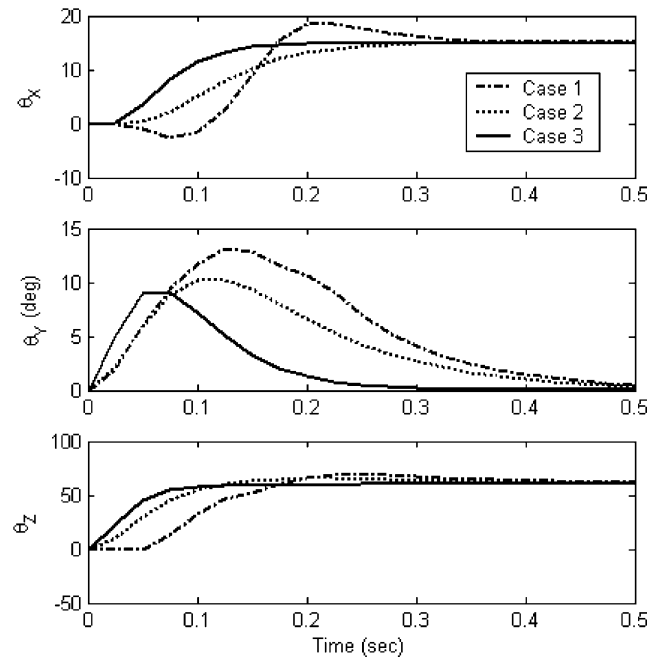


Fig. 12. Comparison of the step responses.

discrepancies between the applied torque and the desired torque for DC-II; indicating that the desired current inputs (calculated from the desired torque) significantly exceed the current limit of 3.75 A during the transient. As shown in Figs. 13(b) and (c), the DC-III was able to deliver the torque as required due to a larger number of coils and a better arrangement of the coils and PM poles.

As seen in Fig. 14, the persistent demand of a saturated torque for the DC-II could result in overheating the motor. Thanks to the linearity of the torque model, which would allow for a large number of highly distributed inputs to be used without the penalty of computational burdens. The result is that much lower heat energy is dissipated during the transient provided that the final position can be maintained mechanically, a research topic being studied.

The heat generated by the copper wire on the stator coils should be effectively dissipated. An effective way is to construct the stator shell and the cores of stator coils out of aluminum so that the heat from the copper wire can be conducted through the

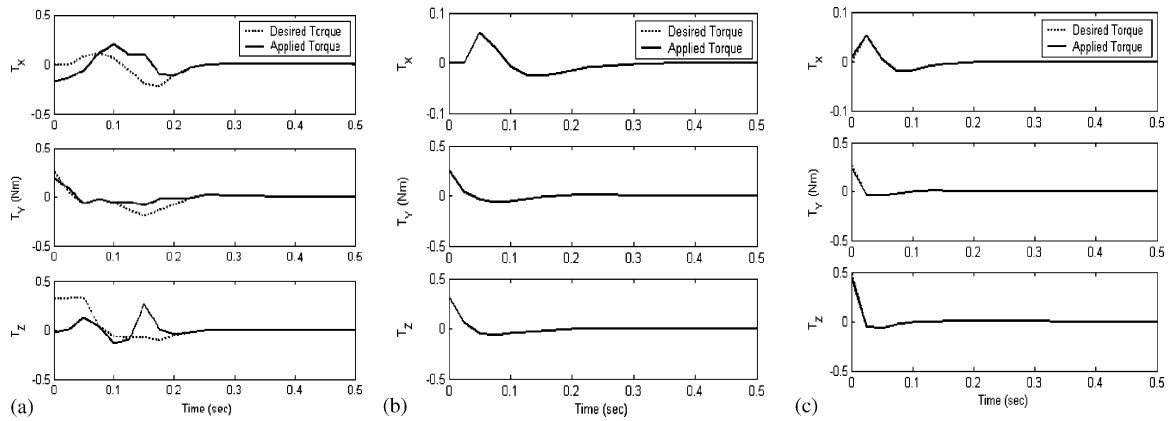


Fig. 13. Desired and applied torque. (a) Case 1 (b) Case 2 (c) Case 3.

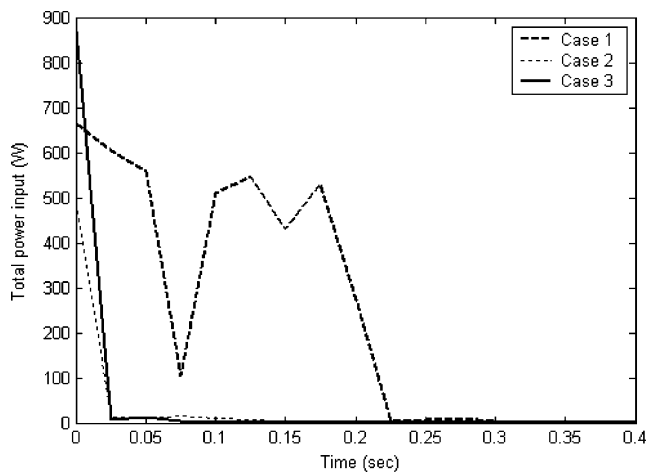


Fig. 14. Total power of heat dissipation during the transient.

aluminum core to the aluminum shell that acts as a large heat sink, where the surface is cooled by means of natural convection. Fig. 15 shows the ANSYS simulated temperature distribution of DC-III using the time average power input in Case 3. As shown in the sectional view (Fig. 15) that cut through a pair of stator coils, the heat is effectively dissipated via conduction as shown in the figure.

7. Conclusions

A general form of the torque model for a VRSM has been derived from the principle of energy conversion. The torque models for two specific design configurations developed at Georgia Tech have been

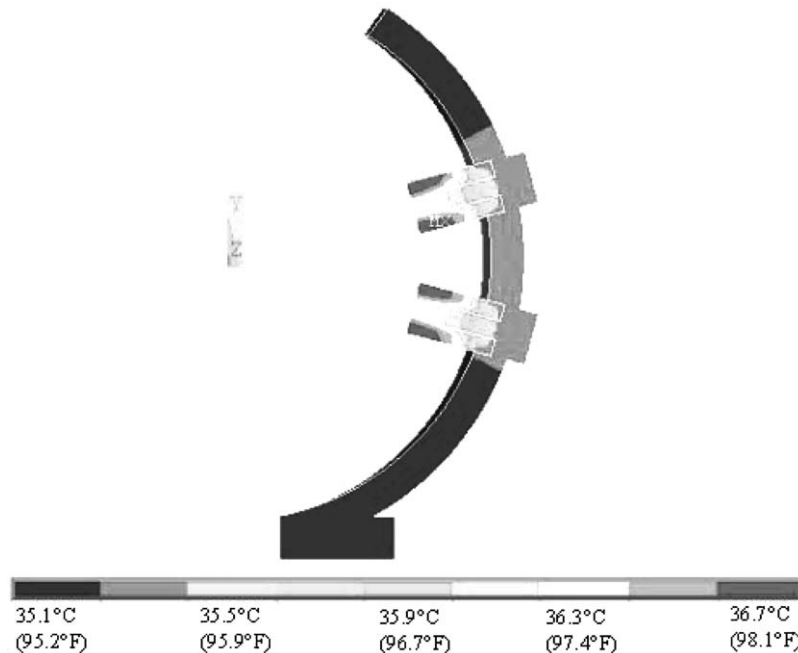


Fig. 15. Temperature distribution of DC-III (simulation using time average power input).

compared — one with a quadratic model and the other with a linear torque model. Using ANSYS, an off-the-shelf FE code, we verified the numerically computed torque using DC-I. The torque model for DC-II has been derived using the 3D FE computation for the second design.

Along with the torque model, a complete dynamic model that takes into account the effects of the orientation measurement system has been employed to serve as a design tool to simulate the dynamic performance of a PD-controlled VRSM system. Experiments conducted on a VRSM prototype shows that experimental results agree well with the computation derived analytically. We expect that the dynamic model that includes both forward and inverse torque models will provide a useful platform for tuning of the controller gains of the VRSM control system.

Through a design simulation of a third design configuration (DC-III), we show that a linear torque model (which ease the large number of highly distributed inputs to be used without the penalty of computational burdens) could result in much lower heat energy dissipated during the transient.

Acknowledgements

We appreciate Debao Zhou, Jeffry Joni, and John Graham for their help in fabricating the rotor of DC-II.

References

- Chirikjian, G. S. & Stein, D. (1999). Kinematic design and commutation of a spherical stepper motor. *IEEE/ASME transactions on mechatronics*, Vol. 4, no. 4. Piscataway, New Jersey, pp. 342–353.
- Davey, K., Vachtsevanos, G. J., & Powers, R. (1987). An analysis of fields and torques in spherical induction motors. *IEEE Transactions on Magnetics*, MAG-23, 273–282.
- Foggia, A., Oliver, E., & Chappuis, F. (1988). New three degrees of freedom electromagnetic actuator. *Conference record—IAS annual meeting*, Vol. 35, New York.
- Hollis, R. L., Salcudean, S. E., & Allan, A. P. (1991). A six-degree-of-freedom magnetically levitated variable compliance fin-motion wrist: Design, modeling, and control. *IEEE Transactions on Robotics and Automation*, 7(3), 320–332.
- Kaneko, K., Yamada, I., & Itao, K. (1988). A spherical DC servo motor with three degrees of freedom. *ASME, dynamic system and control division*, pp. 398–402.
- Lee, K.-M. & Pei, J. (1991). Kinematic analysis of a three degrees of freedom spherical wrist actuator. *Proceedings of the fifth International conference on advanced robotics*, Italy.
- Lee, K.-M., Roth, R., & Zhou, Z. (1996). Dynamic modeling and control of a ball-joint-like VR spherical motor. *ASME Journal of Dynamic Systems, Measurement and Control*, 118(1), 29–40.
- Lee, K.-M., Vachtsevanos, G. J., & Kwan, C.-K. (1988). Development of a spherical wrist stepper motor. *Proceedings of ICRA'88*, April 26–29, Philadelphia, PA.
- Sosseh, R. A., (2001). Finite element torque modeling and backstepping control of a spherical motor. *Ph.D. Dissertation*, George W. Woodruff School of Mechanical Engineering, Georgia Institute of Technology, November 2001.
- Wang, J., Jewel, G., & Howe, D. (1997). Modeling of a novel spherical permanent magnet actuator. *Proceedings of ICRA'97*. Albuquerque, New Mexico, pp. 1190–1195.